

See discussions, stats, and author profiles for this publication at: <https://www.researchgate.net/publication/43519776>

ZnO Films Grown on Si Substrates with Au Nanocrystallites as Nuclei

ARTICLE *in* CRYSTAL GROWTH & DESIGN · MARCH 2007

Impact Factor: 4.89 · DOI: 10.1021/cg060237s · Source: OAI

CITATIONS

8

READS

26

9 AUTHORS, INCLUDING:



Junyong Kang

Xiamen University

221 PUBLICATIONS 1,945 CITATIONS

SEE PROFILE

ZnO Films Grown on Si Substrates with Au Nanocrystallites as Nuclei

Xia Feng,[†] Junyong Kang,^{*,†,‡} Wataru Inami,^{§,#} Xiaoli Yuan,^{||} Masami Terauchi,[§] Takashi Sekiguchi,^{||} Shin Tsunekawa,[⊥] Shun Ito,[⊥] and Toshio Sakurai[‡]

Department of Physics and Photonics Research Center, Xiamen University, Xiamen 361005, P. R. China, International Frontier Center for Advanced Materials, Tohoku University, Japan, Institute of Multidisciplinary Research for Advanced Materials, Tohoku University, Japan, Nanomaterials Laboratory, National Institute for Materials Science, Tsukuba, Japan, and Institute for Materials Research, Tohoku University, Japan

Received April 20, 2006; Revised Manuscript Received November 28, 2006

ABSTRACT: ZnO films were grown on Si substrates with Au nanocrystallites at different temperatures. The morphologies of Au at different annealing temperatures suggest that Au nanocrystallites can perform in the role of crystal nucleus. Surface morphologies of as-grown ZnO films were characterized as a number of hexagonal heaps in the size range of 3–5 μm by scanning electron microscopy. X-ray diffraction data support the theory that the ZnO grains are well-aligned in the *c*-axis. Cathodoluminescence mappings show that the ultraviolet emission at the band edge is suppressed on top of the hexagonal heap in which the green band is intense. The red shift of the E_2 mode demonstrates that the ZnO films in our work are under a weak tensile stress. This should be attributed to the effect of Au nanocrystallites. The convergent beam electron diffraction (CBED) patterns further reveal that the ZnO films grow in Zn-polar. An ab initio simulation agrees well with the results obtained from the CBED images and provides an intrinsic geometry of the growth of ZnO films.

Introduction

Zinc oxide and its compounds have wide direct band gaps and large exciton binding energies, which are promising for applications in ultraviolet (UV) laser diodes, UV-blue light emitting diodes, solar cells, flat panel displays, surface acoustic wave devices, and chemical sensors.^{1–3} The performance of the applications is very sensitive to the crystal structure, stress, and polarity that are closely related to the growth techniques, conditions and processes, substrates, and buffer layers. Various growth techniques have been hitherto used for the growth of ZnO films on different substrates, such as sapphire, GaN, ZnO, and Si.^{4–6} Because of the lack of an inversion center in wurtzite structure, ZnO films with [0001] or [000 $\bar{1}$] orientation exhibit distinct different polarities which are known to affect optical⁷ and electrical properties⁸ and doping efficiency.^{9,10} Recently, polarity-controllable ZnO films have been grown on sapphire substrates.^{11,12} Because of superior performance in Si technology and the monolithic integration for large-scale optoelectronic devices, the growth of ZnO film is more significant on a Si substrate. However, a large lattice mismatch and an amorphous SiO_x layer on Si surfaces lead to defect formation, poor electrical contact, and misalignment of (0002) growth direction, such as the stacking mismatch and inversion domain boundaries. To control the crystal growth on the Si substrate, different buffer layers have been used for ZnO film epitaxy.^{13–16} Using Au may improve the electrical contact between ZnO film and Si substrate. In this work, we experimentally prove for the first

time that the ZnO films grown on Si substrates with Au layers are along the *c*-axis and in Zn-polar. And the Au nanocrystallites play an important role in reducing the biaxial stress rising from the lattice mismatch between ZnO films and Si substrates.

Experimental Section

ZnO films were grown on Si substrates with the Au layers. The substrates were prepared from Si wafer and cleaned by a standard RCA cleaning procedure. The Au layers were deposited first on the Si substrates at room temperature under an Ar atmosphere, using a radio frequency magnetron sputtering system. The layer thickness was about 15 nm prepared with a sputtering power of 100 W. Then the substrate was put into a quartz boat with the Au layer facing downward above a Zn powder source at a vertical distance of about 5 mm. The furnace temperature was elevated at a rate of 100 $^{\circ}\text{C}/0.1$ h. The growth temperature was varied in a range of 600–1000 $^{\circ}\text{C}$. At the growth temperature, the ZnO film was grown under a N_2 flow rate of 500 sccm with a trace of O_2 of about 0.05 sccm for 2 h. Then the furnace was cooled down quickly to room temperature.

As-grown films were characterized to understand the influence of the Au layer. Their crystallographic characterizations were investigated by X-ray diffraction (XRD, Rigaku Rotaflex D/max-C). Morphology and composition of the surfaces were measured using a scanning electron microscope (SEM, LEO 1530 FESEM) equipped with an energy-dispersive X-ray spectroscopy (EDS). Monochromatic cathodoluminescence (CL) was imaged at room temperature using a thermal field emission SEM (Hitachi S4200), equipped with a CL system (Horiba, MP32). Additionally, Raman scattering experiments were performed using a micro-Raman spectrometer (Renishaw, inVia RIA Microscope) with a HeNe laser (633 nm) as the excitation source. The spectra were recorded in backscattering configurations when the incident light is normal to the sample surface. For cross-sectional investigation with a transmission electron microscope, specimens were cut out from the samples, glued face to face, mechanically ground down to about 100 μm thickness, dimpled down to about 10 μm thickness, and finally thinned with Ar^+ ions at 1.5 kV. The polarities of the ZnO films were determined by convergent beam electron diffraction (CBED) with a transmission electron microscope (TEM, JEOL JEM-2010) at 200 kV. The CBED patterns are obtained in several regions of different samples with a probe of about 20 nm.

* To whom correspondence should be addressed. Tel.: +86-592-2185962; Fax: +86-592-2182810. E-mail: jykang@xmu.edu.cn.

[†] Xiamen University.

[‡] International Frontier Center for Advanced Materials, Tohoku University.

[§] Institute of Multidisciplinary Research for Advanced Materials, Tohoku University.

^{||} National Institute for Materials Science.

[⊥] Institute for Materials Research, Tohoku University.

[#] Present address: System Development Division, JEOL Ltd., 3-1-2 Musashino, Akishima, Tokyo 196-8558, Japan.

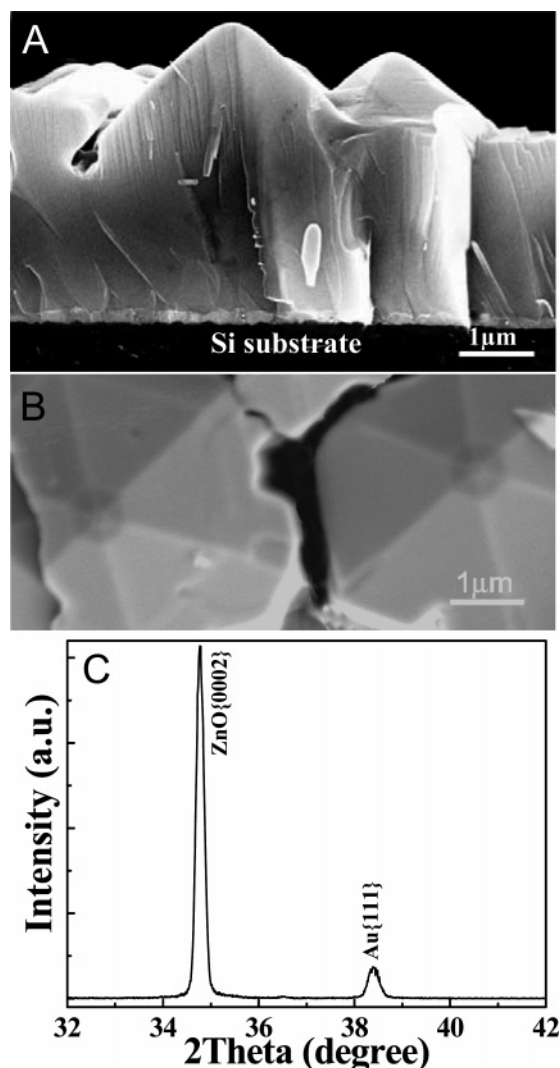


Figure 1. SEM section-view (A) and plane-view (B) images and XRD patterns (C) of ZnO film at a growth temperature of 700 °C.

Results and Discussion

ZnO films were observable when the growth temperatures were higher than 700 °C. The morphologies of the as-grown ZnO thin films grown at different temperatures were similar. The SEM section-view image of ZnO at a growth temperature of 700 °C, as shown in Figure 1A, shows a film comprised of single-crystal hexagonal crystallite heaps. The thickness of the ZnO film was in the range of 2.5–4.1 μm and the height of the heap was about 1.5 μm , which were characterized by a number of hexagonal islands 3–5 μm in diameter as shown in the SEM plane-view images (Figure 1B). These indicate that the crystallite of ZnO grows along the *c*-axis with the multilayer growth mechanism¹⁷ and nucleates on the top before the previous layer is completely formed.

The structures of the ZnO films were determined by XRD. A peak with $2\theta = 34.77^\circ$ is indexed to the wurtzite structure of ZnO {0002} plane in Figure 1C. The full-width at half-maximum (fwhm) of the {0002} peak is 0.175° . Narrow line width of the peak indicates that the films are well-aligned. A small peak of Au (111) planes is also visible, which shows that the Au layer has been well-crystallized.

To discover the role that the Au layer played, we further studied the morphologies of Au films after annealing at 600, 800, and 1000 °C. The heating-up rate was the same as that in

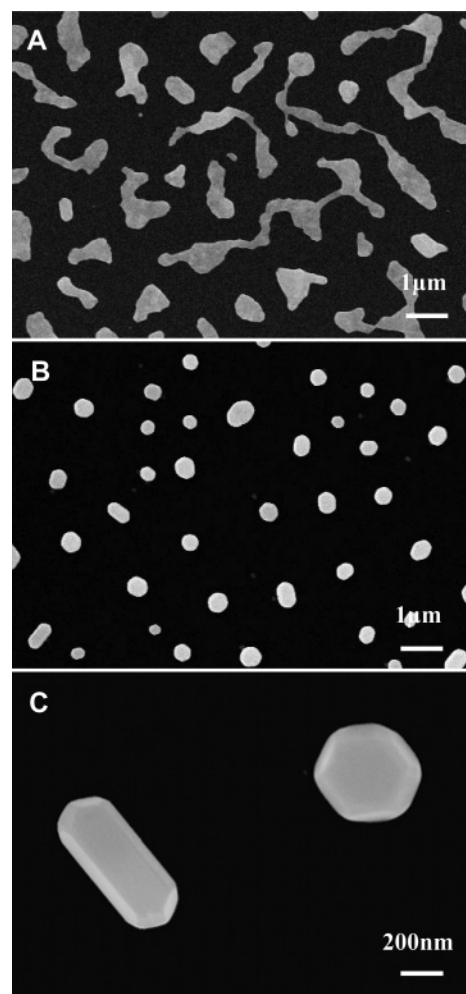


Figure 2. (A, B) SEM images of the annealing samples at 600 and 800 °C, respectively. (C) The magnified SEM image of Figure 2B.

the process of growing ZnO. Figures 2A and 2B are the SEM images of the annealing samples at 600 and 800 °C, respectively. It can be clearly seen that Au has diffused on the surface of Si substrate and existed as shapeless grains at the temperature of 600 °C. While the temperature reached 800 °C, shapeless Au particles became Au nanocrystallites having hexagonal planes, as shown in Figure 2C (the magnified SEM image of Figure 2B). Based on the foregoing description, it is inferred that Au nanocrystallites can perform in the role of crystal nucleus.

It has been known that the cathodoluminescence from semiconductors is generally associated with the crystalline quality. The intensity images represent the defect distribution. CL of the as-grown ZnO film was measured at room temperature. As shown in Figure 3A, the CL spectra exhibit two distinct peaks, a strong peak in the UV region and a broad band in the visible region. The UV emission peaked at about 380 nm is known to originate from the exciton recombination of ZnO. The broad green band emission is attributed to oxygen vacancies or donor–acceptor pair recombination, etc.¹⁸ Typical monochromatic CL images for emissions at 380 and 520 nm are shown in Figures 3B and 3C, respectively, associated with the surface morphology imaged in Figure 1B. The green band is intense on top of all the hexagonal heaps, while the UV emission is suppressed there. If we attribute this emission to oxygen vacancies, it is indicated that the Zn is rich on the top of the

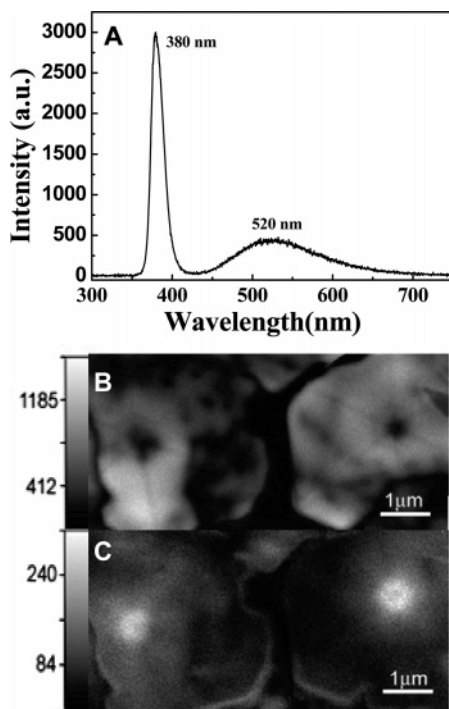


Figure 3. CL spectrum (A) and mappings of emissions at 380 (B) and 520 nm (C), respectively, for the ZnO grains in Figure 1B, operated at an acceleration voltage of 5 kV and a sample current of 120 pA.

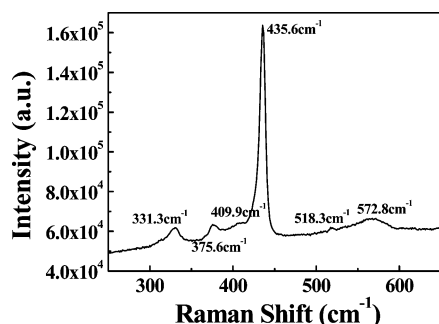


Figure 4. Raman scattering spectrum of the ZnO films at a growth temperature of 700 °C.

heaps where the nuclei initiate. Apart from the top, the UV emission is strong, which shows that the grown layers are well-crystallized.

Raman scattering spectroscopy was carried out in the range of 200–800 cm^{-1} . Several peaks are recognizable at 331.3, 375.6, 435.6, 518.3, and 572.8 cm^{-1} in the spectra, as shown in Figure 4. Except for the Raman peak at 518.3 cm^{-1} originating from Si substrate, the other peaks are associated with the ZnO films.¹⁹ Since the crystalline structure of the ZnO films is a wurtzite type, the optical phonons at the Γ -point of the Brillouin zone belong to the following irreducible representation:²⁰ $\Gamma = A_1 + 2E_2 + E_1$, where both the A_1 and E_1 modes are polar and capable of splitting into transverse optical (TO) and longitudinal optical (LO) phonons. E_2 mode is nonpolar and Raman-active. In the backscattering geometry of this work, the z -direction is normal to the sample surface and parallel to the c -axis, and thus only the E_2 and $A_1(\text{LO})$ modes are observable because the E_2 phonon is allowed in both $z(xy)z'$ and $z(xx)z'$ configurations by the selection rules, in contrast with the $A_1(\text{LO})$ phonon allowed only in the $z(xx)z'$ configuration. In light of these, the strongest peak at 435.6 cm^{-1} is assigned as the E_2

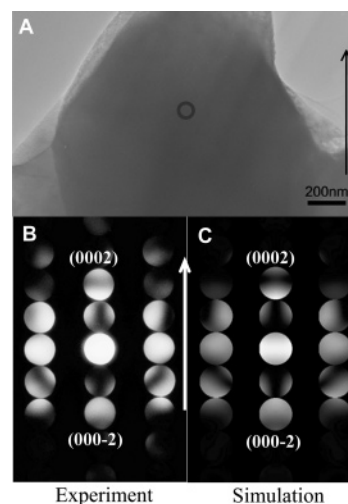


Figure 5. (A) TEM image of a ZnO grain with the growth direction indicated by an arrow. (B) Experimental CBED patterns obtained in the region circled in (A). (C) Simulated CBED patterns for a wurtzite ZnO with a 3.750 μm thickness and Zn polarity.

mode, which is characteristic of wurtzite-type phase of ZnO, and the broad peak at 572.8 cm^{-1} is consistent with $A_1(\text{LO})$ modes. In addition, two forbidden TO modes near 375.6 cm^{-1} (A_1) and 409.9 cm^{-1} (E_1) are apparent. The broad peak at 331.3 cm^{-1} is believed to be attributed to the second-order Raman process. Generally, the appearance of the forbidden $A_1(\text{TO})$ and $E_1(\text{TO})$ modes can be attributed to the increasing contribution of scattering off the facets or sidewalls of the grains.²¹ However, the intense E_2 mode accompanied by the weak $A_1(\text{TO})$ and $E_1(\text{TO})$ modes also shows the ZnO films to be well-aligned in the c -axis.

It is known that shifts in the E_2 mode can be associated with residual film stress.²⁰ The pressure dependence of a normal-mode frequency is described in terms of a so-called “mode Grüneisen parameter” defined by $\gamma_i = -(d\ln\nu_i/d\ln V)_{P=0} = B_0 d\nu_i/(v_i dP)$, where $B_0 = 170$ GPa.²² For the high-frequency E_2 mode of ZnO, $\gamma_i = 1.84$.²² In our work, the frequency of the E_2 mode is 1.4 cm^{-1} lower than 437 cm^{-1} of the bulk ZnO crystal.²³ If the red shift of the E_2 mode does not arise from the measurement error, the ZnO films in our work are under a weak tensile stress of about 0.3 GPa, which is much weaker than the stress of the large lattice mismatch between ZnO ($a_0 = 3.24$ Å) and Si(111) ($a = 3.82$ Å). The weaker stress in our samples should be attributed to the effect of Au nanocrystallites.

Moreover, the amount of TO–LO splitting for the A_1 and E_1 modes depends on the long-range electrostatic forces, which should be diminished if the phonons are localized by point defects. In our case, both the $A_1(\text{TO})$ and $A_1(\text{LO})$ modes shift only a little to the low frequencies. This implies that the ZnO films have good crystalline quality.

The above experimental data demonstrate that the crystalline films grow along $\langle 0001 \rangle$, which is consistent with most of the previous reports. However, the c -axis ZnO has two distinct polar planes, (0001) Zn- and (000 $\bar{1}$) O-polar ones. If the neighboring grains have different polarities, the coalescence between them forms imperfections such as inversion domains. CBED has been widely used to determine the polarity of wurtzite-type materials.^{24,25} To understand the polarities of the different regions, the CBED patterns are measured with thickness in the 3.5–22 μm range of different grains. Figure 5A shows a detected region in a ZnO grain with the growth direction indicated by an arrow. The measured CBED patterns of the ZnO film were obtained

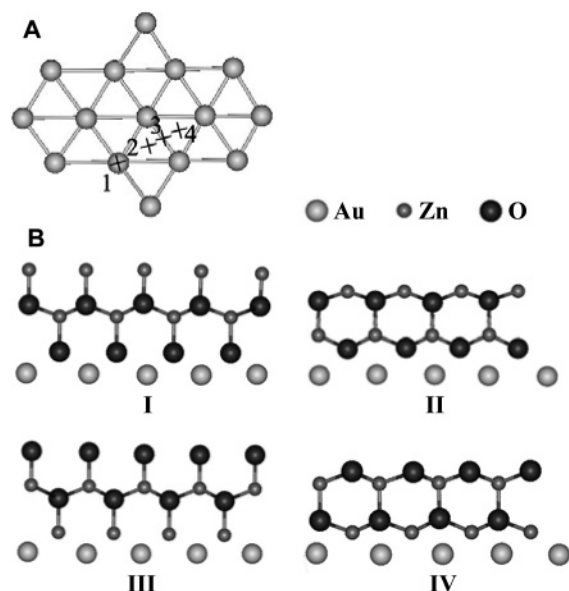


Figure 6. (A) Surface geometry of Au(111) and adsorption sites of Zn or O atoms: (1) on top, (2) hcp, (3) bridge, and (4) fcc. (B) Schematic illustration of the atomic arrangement of wurzite-type {0001} ZnO surfaces: (I) O-polar surface with Zn-atom termination, (II) Zn-polar surface with Zn-atom termination, (III) Zn-polar surface with O-atom termination, and (IV) O-polar surface with O-atom termination.

from several regions per sample with the zone axis of $[2\bar{1}10]$. The experimental CBED pattern (Figure 5B) was in good agreement with the simulation pattern for a specimen thickness of $3.750\ \mu\text{m}$ (Figure 5C). The simulated pattern reveals that epitaxial growth (pointed out by an arrow) is along the (0001) direction. The comparison results for different specimen thicknesses all show that the ZnO grains are of Zn polarity. This indicates that the Au nanocrystallites can be used to control Zn polarity for the ZnO films grown on Si.

The growth habit of crystals is determined by internal structure and also is affected by external conditions. To find out what affects the growth habit and the polarity of the ZnO crystalline films, first-principles calculations based on the density functional theory were performed to investigate the initial growth of ZnO films on Au layer using the “Vienna ab initio simulation package” (VASP).^{26–28} As a basis for the calculations, the geometry of Au surfaces was optimized first and the equilibrium lattice constant a_0 was obtained to be $4.05\ \text{\AA}$, which agrees well with the experimental value $4.07\ \text{\AA}$.^{29,30} The surface of Au was assumed to be {111} planes from the XRD pattern (see Figure 1B). A slab with seven atomic layers was used.

A monolayer of Zn or O atoms was placed onto the optimized Au surface. Four possible adsorption sites (on top, hcp, bridge, and fcc sites) were considered for the Zn or O atoms as shown in Figure 6A. The energy on each site was obtained after the relaxation of atoms. The energies increase in the sequence hcp, fcc, bridge, and on-top sites, whether Zn or O atoms are on the Au surface. As a result, the hcp site can be considered as an initial growth site for the ZnO films. To simulate the combining sequence of the Zn and O atoms in the ZnO molecules on the Au surface, four configurations with the same number of Zn and O atoms in one supercell have been considered on the Au (111) surface, as shown in Figure 6B: (I) O-polar surface with Zn-atom termination, (II) Zn-polar with Zn termination, (III) Zn-polar with O termination, and (IV) O-polar with O termination. After the relaxation of the Au surface and the four layers of Zn and O atoms, the total energies of the four configurations were obtained: -44.586 , -44.781 , -48.169 , and $-47.864\ \text{eV}$,

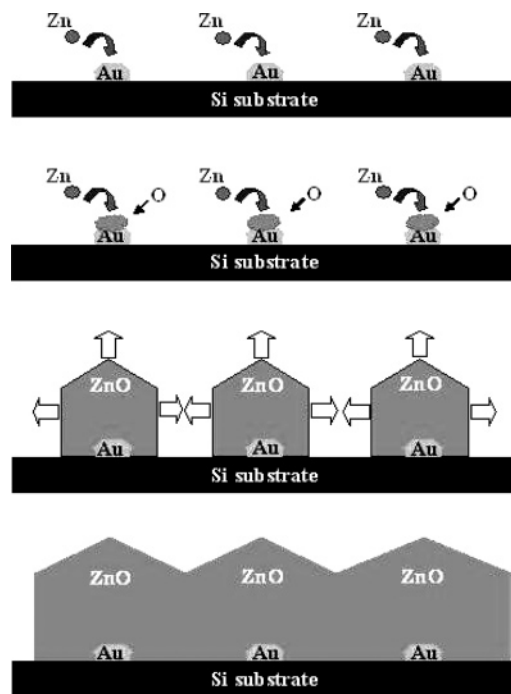


Figure 7. Schematic illustration of the proposed growth mechanism.

respectively. This indicates that the configuration III is energetically favorable for the initial growth in which the Zn atoms are first adsorbed on the Au surface and then the O atoms are stabilized on the top sites of the Zn atoms, leading to Zn-polar ZnO films. This result coincides with the CBED analysis and provides an intrinsic geometry of the ZnO film growth along the c -axis.

On the basis of the above experimental and theoretical results, a growth mechanism is proposed to explain the nucleation and growth processes of the ZnO films on the Au nanocrystallites, as shown in Figure 7. The presence of the Au layer disappeared after the Au–Si eutectic temperature of $365\ ^\circ\text{C}$ was crossed. When the temperature was higher than $700\ ^\circ\text{C}$, Au nanocrystallites formed. The vaporized Zn was carried by the processing gas and deposited on the surface of Au nanocrystallites. The Zn nucleates first and then was oxidized, which results in the formation of point defects in nuclei such as O vacancies and Zn interstitials. Due to the mismatch between the ZnO and Au nanocrystallites, the ZnO grains endure a compression stress during the growth. While the nuclei grew gradually to the side, Zn and O reach the stoichiometric ratio. The islands of ZnO joined together and then formed a ZnO film of good quality. According to Laudise’ argument on the growth of polar crystals,³¹ the growth rate along the (0001) direction is the fastest, and the (0001) faces disappear in the end. The process repeats itself with nucleation and growth on the top of hexagonal heaps.³² Because the nucleation of each ZnO layer occurs on the top of the islands, which was dominated by Zn adsorption, the point defects due to the insufficient oxidation in the Zn nuclei are concentrated on the top.

Conclusion

ZnO films were grown on the Si substrates with Au nanocrystallites. The CL mapping shows that the UV emission at the band edge is suppressed on the top of the hexagonal crystallite heaps where the green band is intense. The Raman scattering measurements demonstrate that the ZnO films grow well along the c -axis and undergo the weaker misfit stress. The

CBED patterns further show that the ZnO films are of Zn polarity. The first-principles calculations provide an intrinsic geometry of the formation of the Zn-polar ZnO film. With use of Au, not only the misfit stress has been minimized and Zn-polarity has been controlled but also electrical and thermal conductivities between the ZnO films and the Si substrates could be improved. However, many works await further investigation.

Acknowledgment. This work was partly supported by the Special Funds for Major State Basic Research Projects (Grant No. 2001CB610505), the National Nature Science Foundation (Grant Nos. 60376015, 60336020, 90206030, and 10134030), and the grants (2004H054 and E0410007) from Fujian Province in China.

References

- (1) Bagnall, D. M.; Chen, Y. F.; Zhu, Z.; Yao, T.; Shen, M. Y.; Goto, T. *Appl. Phys. Lett.* **1998**, *73*, 1038.
- (2) Huang, M. H.; Mao, S.; Feick, H.; Yan, H.; Wu, Y.; Kind, H.; Weber, E.; Russo, R.; Yang, P. *Science* **2001**, *292*, 1897.
- (3) Lee, C. J.; Lee, T. J.; Lyu, S. C.; Zhang, Y.; Ruh, H.; Lee, H. J. *Appl. Phys. Lett.* **2002**, *81*, 3648.
- (4) Ko, H. J.; Yao, T.; Chen, Y.; Hong, S. K.; *J. Appl. Phys.* **2002**, *92*, 4354.
- (5) Ogata, K.; Kawanishi, T.; Maejima, K.; Sakurai, K.; Fujita, S.; Fugita, S. *J. Cryst. Growth* **2002**, *237–239*, 553.
- (6) Jeong, S. H.; Kim, I. S.; Kim, J. K.; Lee, B. T. *J. Cryst. Growth* **2004**, *264*, 327.
- (7) Kirilyuk, V.; Zauner, A. R. A.; Christianen, P. C. M.; Weyher, J. L.; Hageman, P. R.; Larsen, P. K. *Appl. Phys. Lett.* **2000**, *76*, 2355.
- (8) Dimitrov, R.; Murphy, M.; Smart, J.; Schaff, W.; Shealy, J. R.; Eastman, L. F.; Ambacher, O.; Stutzmann, M. *J. Appl. Phys.* **2000**, *87*, 3375.
- (9) Li, L. K.; Jurkovic, M. J.; Wang, W. I.; Van Hove, J. M.; Chow, P. *Appl. Phys. Lett.* **2000**, *76*, 1740.
- (10) Look, D. C.; Reynolds, D. C.; Litton, C. W.; Jones, R. J.; Eason, D. B.; Cantwell, G. *Appl. Phys. Lett.* **2002**, *81*, 1830.
- (11) Mei, Z. X.; Du, X. L.; Wang, Y.; Ying, M. J.; Zeng, Z. Q.; Zheng, H.; Jia, J. F.; Xue, Q. K.; Zhang, Z. *Appl. Phys. Lett.* **2005**, *86*, 112111.
- (12) Wang, X. Q.; Tomita, Y.; Roh, O.-H.; Ohsugi, M.; Che, S.-B.; Ishitani, Y.; Yoshikawa, A. *Appl. Phys. Lett.* **2005**, *86*, 011921.
- (13) Frank, T.; Smith, J. *Appl. Phys. Lett.* **1983**, *43*, 1108.
- (14) Iwata, K.; Fons, P.; Niki, S.; Yamada, A.; Matsubara, K.; Nakahara, K.; Tanabe, T.; Takasu, H. *J. Cryst. Growth* **2000**, *214/215*, 50.
- (15) Fu, Z. X.; Lin, B. X.; Liao, G. H.; Wu, Z. Q. *J. Cryst. Growth* **1998**, *193*, 316.
- (16) Joseph, M.; Tabata, H.; Saeki, H.; Ueda, K.; Kawai, T. *Physica B* **2001**, *302–303*, 140.
- (17) Tersoff, J.; Denier van der Gon, A. W.; Tromp, R. M. *Phys. Rev. Lett.* **1994**, *72*, 266.
- (18) Vanheusden, K.; Warren, W. L.; Seager, C. H.; Tallant, D. K.; Voigt, J. A.; Gnade, B. E. *J. Appl. Phys.* **1996**, *79*, 7983.
- (19) Zhang, Y.; Jia, H. B.; Wang, R. M.; Chen, C. P.; Luo, X. H.; Yu, D. P.; Lee, C. *Appl. Phys. Lett.* **2003**, *83*, 4631.
- (20) Arguello, C. A.; Rousseau, D. L.; Porto, S. P. S. *Phys. Rev.* **1969**, *181*, 1351.
- (21) Wang, Y. D.; Chua, S. J.; Tripathy, S.; Sander, M. S.; Chen, P.; Fonstad, C. G. *Appl. Phys. Lett.* **2005**, *86*, 071917.
- (22) Decremps, F.; Porres, J. P.; Saitta, A. M.; Chervin, J. C.; Polian, A. *Phys. Rev. B* **2002**, *65*, 092101.
- (23) Ashkenov, N.; Mbenkum, B. N.; Bundesmann, C.; Riede, V.; Lorenz, M.; Spemann, D.; et al. *J. Appl. Phys.* **2003**, *93*, 126.
- (24) Ramachandran, V.; Feenstra, R. M.; Samey, W. L.; alamanca-Riba, L.; Northrup, S. J. E.; Romano, L. T.; Greve, D. W. *Appl. Phys. Lett.* **1999**, *75*, 808.
- (25) Romano, L. T.; Northrup, J. E.; Ptak, A. J.; Myers, T. H. *Appl. Phys. Lett.* **2000**, *77*, 2479.
- (26) Kresse, G.; Furthmuller, J. *Phys. Rev. B* **1996**, *54*, 11169.
- (27) Kresse, G.; Furthmuller, J. *Comput. Mater. Sci.* **1996**, *6*, 15.
- (28) Kresse, G.; Hafner, J. *Phys. Rev. B* **1993**, *47*, 558.
- (29) Kittel, C. *Introduction to Solid State Physics*; Wiley: New York, 1996.
- (30) Wang, L. L.; Cheng, H. P. *Phys. Rev. B* **2004**, *69*, 165417.
- (31) Laudise, R. A.; Ballman, A. A. *J. Phys. Chem.* **1960**, *64*, 688.
- (32) Baxter, J. B.; Wu, F.; Aydil, E. S. *Appl. Phys. Lett.* **2003**, *83*, 3797.

CG060237S